Biogenic synthesis, characterization, antimicrobial and photocatalytic studies of zinc oxide nanoparticles prepared using neem and moringa leaf aqueous extracts

Masokano, D.S.A.[1*], **Alkali, M.D.**[1], **Salawu, O.W.**[1], **Lawal, U.**[2] and **Yahaya, M.K.**[3]

[1]Department of Chemistry, Federal University Lokoja, P.M.B. 1154, Lokoja, Kogi State, Nigeria

[2]Department of Chemistry, Air Force Institute of Technology, Kaduna, Nigeria

[3]Department of Chemistry, Confluence University of Science and Technology, Osara, Kogi State, Nigeria

***Corresponding author:** Masokano D.S.A. (dailami.adam@fulokoja.edu.ng; Tel: +234 706 649 5355)

Cite this article as: Masokano, D.S.A., Alkali, M.D., Salawu, O.W., Lawal, U. and Yahaya, M.K. (2026). Biogenic synthesis, characterization, antimicrobial and photocatalytic studies of zinc oxide nanoparticles prepared using neem and moringa leaf aqueous extracts. *Journal of Interdisciplinary Postgraduate Research*, **1**(1), 42-67.

Abstract

The drive towards sustainability and green nanotechnology has sparked increasing interest in the development of environmentally benign processes for synthesis of nanomaterials, especially using plant aqueous extracts as capping and reducing agents. In this study, two zinc oxide nanoparticle samples were fabricated using leaf aqueous extracts of neem (ZnO NLE) and moringa (ZnO MLE) as bio reducing and stabilizing agents. Successful synthesis was confirmed using comprehensive characterization techniques including Fourier transform infrared spectroscopy, x ray diffraction, ultraviolet visible spectroscopy, thermogravimetric analysis, scanning electron microscopy, transmission electron microscopy, and energy dispersive x ray spectroscopy. Fourier transform infrared spectroscopy revealed zinc oxygen vibrations alongside organic residues from leaf phytochemicals, while x ray diffraction confirmed hexagonal wurtzite crystal structures with crystallite sizes of 24.5 nanometres for ZnO NLE and 17.5 nanometres for ZnO MLE, as determined using Scherrer equation. Ultraviolet visible spectroscopy results indicated strong ultraviolet light absorption characteristics and optical band gaps of 2.98 and 3.02 electron volts respectively, estimated using Tauc plot method. Scanning electron microscopy images showed quasi spherical morphology with moderate agglomeration for ZnO NLE, while ZnO MLE sample revealed smaller and more densely clustered nanoparticles. Transmission electron microscopy images confirmed these morphological observations, with ZnO MLE showing broader particle size distribution compared to ZnO NLE, and average particle sizes of 35 nanometres for ZnO NLE and 28 nanometres for ZnO MLE. The biosynthesized samples were systematically tested for antimicrobial and photocatalytic applications. Antimicrobial assay results demonstrated that ZnO NLE possesses stronger antibacterial properties, particularly against Bacillus subtilis and Pseudomonas aeruginosa, with minimum inhibitory concentration values as low as 25 milligrams per millilitre. In contrast, ZnO MLE showed limited antifungal activity and required higher minimum inhibitory concentrations. Photocatalytic degradation studies of organic dyes under natural solar irradiation revealed that ZnO MLE is a more efficient photocatalyst, achieving 34 and 35 percent degradation of methyl orange and Congo red dyes respectively within 120 minutes, with pseudo first order rate constants of 0.0044 and 0.0046 inverse minutes. These comprehensive results demonstrate that ZnO NLE is a more promising antimicrobial agent while ZnO MLE exhibits greater potential as a photocatalyst, thereby emphasizing the critical role of plant phytochemicals in tailoring functional properties of zinc oxide nanoparticles toward specific applications.

Keywords: zinc oxide; nanoparticle; biosynthesis; plant extract; phytochemicals; photocatalyst; antimicrobial; green chemistry; sustainable nanotechnology; Azadirachta indica; Moringa oleifera.

1. Introduction

Nanomaterials development has revolutionized numerous fields, offering innovative solutions across science, technology, and engineering disciplines *(Malik et al., 2023)*. The unique physicochemical properties of nanomaterials arising from their nanoscale dimensions (typically 1 to 100 nanometres), combined with exceptional optical, electrical, mechanical, and catalytic characteristics, enable their widespread application in diverse areas including medicine, environmental remediation, energy conversion and storage, agriculture, and advanced manufacturing *(Roy et al., 2024)*.

Nanomaterials can be broadly classified based on several criteria: dimensionality (zero dimensional quantum dots, one dimensional nanowires and nanotubes, two dimensional nanosheets, and three dimensional nanostructured materials), chemical composition (metallic nanoparticles, metal oxide nanoparticles, carbon based nanomaterials, and polymer nanocomposites), and morphological characteristics (nanoparticles, nanorods, nanoflowers, nanosheets, nanofibers, and hierarchical nanostructures). The synthesis methodology employed is critical, as it directly determines the shape, size distribution, surface area, crystallinity, and ultimately the functional properties of the resulting nanomaterials *(Ahmed et al., 2017)*.

Traditional synthesis approaches encompass top down methods (mechanical milling, lithography, etching), bottom up methods (chemical vapor deposition, sol gel synthesis, hydrothermal routes, microemulsion techniques), and physical methods (laser ablation, sputtering, evaporation condensation). However, many conventional chemical synthesis routes involve the use of toxic chemical reducing agents, organic solvents, and high energy demanding reaction conditions, which raise significant environmental and safety concerns *(Alsaiari, 2023)*.

Recently, green synthesis or biogenic synthesis approaches utilizing biological resources such as plant extracts, bacteria, fungi, algae, and other biomolecules have gained substantial prominence as environmentally sustainable alternatives. These biocompatible synthesis routes avoid the utilization of hazardous chemicals and harsh reaction conditions characteristic of conventional methods *(Yadav et al., 2024)*. In plant mediated (phyto assisted or biogenic) synthesis, diverse phytochemicals including polyphenols, flavonoids, terpenoids, alkaloids, proteins, and reducing sugars act synergistically as reducing, capping, and stabilizing agents for metal ions during nanoparticle formation. On the other hand, microbial synthesis employs bacteria or fungi to bioreduce metal ions either intracellularly or extracellularly through enzymatic processes. Both methods are termed green synthesis as they generate minimal hazardous byproducts and operate under mild conditions *(Ahmed et al., 2017; Alsaiari, 2023)*.

Zinc oxide is a versatile semiconductor nanomaterial possessing exceptional properties including a wide direct band gap (approximately 3.37 electron volts) and high excitation binding energy (approximately 60 millielectron volts at room temperature), making it particularly valuable for optoelectronic, photocatalytic, sensing, and antimicrobial applications *(Sharma et al., 2022; Raha and Ahmaruzzaman, 2022)*. Zinc oxide nanoparticles, with their enhanced surface to volume ratio and quantum confinement effects, exhibit superior catalytic activity, photochemical stability, and biological interactions compared to their bulk counterparts. However, conventional chemical synthesis methods typically involve toxic precursors such as sodium borohydride, hydrazine hydrate, and dimethylformamide, alongside high energy consumption, which limits their environmental sustainability and economic viability *(Sharma et al., 2022)*.

Consequently, biogenic synthesis has emerged as a promising sustainable alternative for zinc oxide nanoparticle production. This approach eliminates the use and generation of hazardous substances by employing plant secondary metabolites as natural reducing, capping, and stabilizing agents *(Perumalsamý, 2024; Aram, 2025)*. Aqueous extracts of various plant parts, particularly leaves, are rich in bioactive compounds including flavonoids (quercetin, kaempferol, rutin), polyphenols (gallic acid, caffeic acid, chlorogenic acid), terpenoids, saponins, and alkaloids, which collectively facilitate the reduction of zinc precursors and stabilization of nanoparticles through their abundant hydroxyl, carbonyl, and amine functional groups *(Upadhyay et al., 2020)*.

Among the diverse plant species investigated for zinc oxide nanoparticle biosynthesis, *Azadirachta indica* (neem) and *Moringa oleifera* (moringa) have shown

particularly promising capabilities due to their exceptionally rich phytochemical profiles *(Venkataraju et al., 2014; Perumalsamý, 2024)*. Neem leaves contain a complex mixture of bioactive compounds including nimbin, nimbolide, nimbidin, azadirachtin, quercetin, and various terpenoids and tannins. Similarly, moringa leaves are extraordinarily rich in flavonoids (quercetin derivatives, kaempferol derivatives), phenolic acids (chlorogenic acid, gallic acid), vitamins (ascorbic acid, tocopherols), and glucosinolates. These diverse metabolites provide strong reducing capabilities and effective capping properties that facilitate controlled nanoparticle synthesis with tailored morphological and functional characteristics *(Perumalsamý, 2024)*.

Previous studies have demonstrated the potential of both neem and moringa extracts for producing zinc oxide nanoparticles with controllable shape, size distribution, and surface chemistry *(Gupta et al., 2018; Ramesh et al., 2021; Gur et al., 2022)*. However, systematic comparative investigations elucidating how different plant phytochemical compositions influence the structural, optical, antimicrobial, and photocatalytic properties of biosynthesized zinc oxide nanoparticles remain relatively limited in the literature. Understanding these structure property performance relationships is crucial for rational design and optimization of biogenic nanoparticles for targeted applications.

Therefore, this research aims to comprehensively compare the physicochemical properties, antimicrobial efficacy, and photocatalytic performance of zinc oxide nanoparticles biosynthesized using neem leaf extract versus moringa leaf extract. The specific objectives include: (i) synthesis and comprehensive characterization of ZnO NLE and ZnO MLE nanoparticles using multiple analytical techniques; (ii) systematic evaluation of their antimicrobial activities against representative bacterial and fungal pathogens; (iii) assessment of their photocatalytic degradation efficiency toward model organic dye pollutants under natural solar irradiation; and (iv) correlation of observed functional performances with structural and compositional characteristics. The insights gained from this comparative study may contribute to knowledge driven optimization of biogenic zinc oxide nanoparticles for practical applications in sustainable agriculture, water treatment, and biomedical technologies relevant to Nigerian and broader African contexts.

2. Materials and Methods

2.1 Collection and preparation of plant materials

Fresh, healthy leaves of *Moringa oleifera* and *Azadirachta indica* were collected during the early morning hours from Kabba town, Kabba Bunu Local Government Area of Kogi State, Nigeria (coordinates: 7.8250° N, 6.0778° E). Plant specimens were identified and authenticated by a botanist at the Herbarium of the Department of Plant Science and Biotechnology, Federal University Lokoja, where voucher specimens (FUL/BOT/2024/087 for neem and FUL/BOT/2024/088 for moringa) were deposited for future reference. The freshly collected leaves were thoroughly washed multiple times with tap water to remove surface dirt and dust particles, followed by triple rinsing with distilled water to ensure complete removal of contaminants.

The cleaned leaves were spread evenly on clean trays and air dried at ambient room temperature (25 to 28 degrees Celsius) for two weeks in a well ventilated laboratory space, protected from direct sunlight to preserve heat sensitive phytochemicals. Complete drying was confirmed by constant weight measurement. The dried leaves were manually crushed using a clean mortar and pestle, and the resulting powder was sieved through a 200 micrometer mesh laboratory sieve to obtain uniform particle size. The fine powders were stored separately in clean, airtight amber glass bottles and maintained in a cool, dry place away from light until use in nanoparticle synthesis.

2.2 Preparation of leaf aqueous extracts

Aqueous extracts were prepared following established protocols with minor modifications *(Ramesh et al., 2021; Gur et al., 2022)*. Briefly, 50 grams of each prepared leaf powder (neem and moringa separately) was accurately weighed using an analytical balance and transferred to separate 500 millilitre Pyrex glass beakers. To each beaker, 200 millilitres of freshly prepared distilled water was added, and the mixture was placed on a magnetic stirrer hot plate. The suspension was heated to 80 degrees Celsius and maintained at this temperature for 10 minutes under continuous magnetic stirring (500 revolutions per minute) to facilitate maximum extraction of water soluble phytochemicals.

After the heating period, the beakers were removed from the hot plate and allowed to cool naturally to room temperature. The cooled mixtures were then filtered through Whatman Number 1 filter paper using vacuum filtration to obtain clear, particle free extracts. The filtrates, appearing as brownish green solutions due to dissolved chlorophyll and other pigments, were collected in clean conical flasks and used immediately for nanoparticle synthesis to prevent degradation of bioactive compounds. Fresh extracts were prepared for each synthesis batch to ensure consistency and reproducibility.

2.3 Biogenic synthesis of zinc oxide nanoparticles

The biosynthesis of zinc oxide nanoparticles was carried out following green synthesis protocols described in recent literature *(Fang et al., 2014; Ari et al., 2023)*, with appropriate modifications to optimize yield and purity. In this procedure, 20 millilitres of freshly prepared plant leaf aqueous extract (neem or moringa) was measured using a graduated cylinder and transferred into separate 250 millilitre borosilicate glass beakers. Each beaker was then placed on a magnetic stirrer hot plate and heated to 80 degrees Celsius under continuous stirring at 600 revolutions per minute.

Once the extract reached the target temperature, 2.0 grams of analytical grade zinc nitrate hexahydrate ($Zn(NO_3)_2 \cdot 6H_2O$, purity greater than 99 percent, Sigma Aldrich) was accurately weighed and gradually added to the hot extract while maintaining vigorous stirring. The addition of zinc salt to the plant extract resulted in an immediate color change from brownish green to reddish brown, indicating the onset of bioreduction and nanoparticle formation. The reaction mixture was maintained at 80 degrees Celsius for 45 minutes under continuous stirring to ensure complete reduction of zinc ions and formation of stable nanoparticles.

After 45 minutes, a noticeable precipitate formation was observed. The mixtures were then concentrated by heating to remove excess water, cooled to room temperature, and the resulting semi solid mass was transferred to Petri dishes for overnight drying in a vacuum oven maintained at 100 degrees Celsius. The dried solid material was carefully collected, ground into fine powder using an agate mortar and pestle, and transferred to ceramic crucibles for calcination. Calcination was performed in a muffle furnace (Carbolite CWF 1200) at 400 degrees Celsius for 2 hours at a heating rate of 10 degrees Celsius per minute to decompose organic residues and crystallize the zinc oxide phase. The calcined products, obtained as white to off white powders, were labeled as ZnO NLE (zinc oxide from neem leaf extract) and ZnO MLE (zinc oxide from moringa leaf extract), transferred to clean vials, and stored in a desiccator over silica gel until characterization and application studies.

2.4 Characterization techniques

Thermogravimetric analysis was performed using a PerkinElmer STA 6000 simultaneous thermal analyzer. Approximately 10 to 15 milligrams of each sample was loaded into a platinum crucible and heated from 50 to 1000 degrees Celsius at a constant heating rate of 5 degrees Celsius per minute under a flow of air (20 millilitres per minute) to investigate thermal stability and compositional purity of the biosynthesized nanoparticles.

X ray diffraction patterns were obtained using a Bruker D8 Advance multipurpose x ray diffractometer equipped with copper K alpha radiation (wavelength equals 1.5406 angstroms) generated at 40 kilovolts and 45 milliamperes. Diffraction data were collected over a 2 theta range of 5 to 70 degrees with a step size of 0.034 degrees and scan speed of 0.5 seconds per step. Background subtraction and phase identification were performed using the International Centre for Diffraction Data Powder Diffraction File database (PDF 2 Release 1999) and EVA software from Bruker. Crystallite sizes were calculated from the most intense diffraction peaks using the Scherrer equation: D equals K lambda divided by beta cosine theta, where D is crystallite size, K is shape factor (0.9), lambda is x ray wavelength, beta is full width at half maximum, and theta is Bragg angle *(Sharma et al., 2022)*.

Fourier transform infrared spectroscopy was conducted using a PerkinElmer Spectrum 100 spectrometer operating in attenuated total reflectance mode. Spectra were recorded in the wavenumber range of 400 to 4000 inverse centimetres with a resolution of 4 inverse centimetres. Approximately 20 milligrams of each finely ground sample was analyzed after running a background scan to eliminate atmospheric interference. Spectra were baseline corrected and analyzed to identify characteristic functional groups and bonding environments.

Ultraviolet visible diffuse reflectance spectroscopy was performed on an Agilent Cary 5000 ultraviolet visible near infrared spectrophotometer. Samples were prepared by thoroughly mixing approximately 200 milligrams of each zinc oxide sample with an equal mass of barium sulfate (spectroscopic grade) as diluent and reference standard. The homogenized mixture was loaded into a metallic sample holder and spectra were acquired at ambient temperature over a wavelength range of 200 to 700 nanometres with a scan rate of 600 nanometres per minute. Optical band gaps were estimated using the Tauc method by plotting (alpha h nu)^2 versus photon energy (h nu) and extrapolating the linear portion to the energy axis, where alpha is the absorption coefficient *(Ahmed and Edvinsson, 2020)*.

Morphological characterization was conducted using field emission gun scanning electron microscopy (Zeiss Ultra Plus) operated at 5 kilovolts accelerating voltage and various magnifications. Energy dispersive x ray spectroscopy was performed using an Oxford Instruments detector integrated with the scanning electron microscope to determine elemental composition. Samples were prepared by dispersing a small amount of powder on carbon tape adhered to aluminum stubs, followed by platinum coating (approximately 5 nanometres thickness) using a sputter coater to enhance conductivity and image quality.

Transmission electron microscopy imaging was performed using a JEOL JEM 2100 transmission electron microscope operated at 200 kilovolts. Sample preparation involved ultrasonication of approximately 1 milligram of nanoparticle powder in 5 millilitres of absolute ethanol for 10 minutes to achieve good dispersion. A drop of the resulting suspension was placed on a carbon coated copper grid (200 mesh) and allowed to dry under ultraviolet lamp irradiation. Particle size distributions were determined by measuring diameters of at least 100 particles from multiple transmission electron microscopy images using ImageJ software (National Institutes of Health, USA).

2.5 Antimicrobial activity evaluation

The antimicrobial efficacy of biosynthesized zinc oxide nanoparticles was evaluated against two bacterial strains (*Bacillus subtilis* ATCC 6633 and *Pseudomonas aeruginosa* ATCC 27853) and two fungal strains (*Aspergillus fumigatus* ATCC 204305 and *Penicillium* species) using the agar well diffusion method *(Venkataraju et al., 2014; Gupta et al., 2018)*. Pure microbial cultures were obtained from the Microbiology Laboratory, Federal University Lokoja, and maintained on appropriate media.

Stock suspensions of zinc oxide nanoparticles were prepared at a concentration of 100 milligrams per millilitre by dispersing the nanopowders in sterile distilled water followed by ultrasonication for 30 minutes to ensure homogeneous dispersion. Serial dilutions were then performed to obtain working concentrations of 75, 50, and 25 milligrams per millilitre. Mueller Hinton agar was used for bacterial assays and Sabouraud dextrose agar for fungal assays, both prepared according to manufacturer specifications and sterilized by autoclaving at 121 degrees Celsius for 15 minutes.

Microbial inocula were prepared by suspending fresh overnight cultures in sterile saline solution and adjusting turbidity to 0.5 McFarland standard (approximately 1.5 times 10 to the power 8 colony forming units per millilitre). The standardized suspensions were uniformly spread over the entire surface of solidified agar plates using sterile cotton swabs. Wells of 6 millimetres diameter were aseptically created in the inoculated agar using a sterile cork borer. Each well was filled with 100 microlitres of nanoparticle suspension at different concentrations using sterile micropipettes. Chloramphenicol (30 micrograms per disc) and ketoconazole (15 micrograms per disc) served as positive controls for bacteria and fungi respectively, while sterile distilled water was used as negative control.

The plates were allowed to stand at room temperature for 30 to 60 minutes to permit diffusion of nanoparticles into the agar, then incubated at 37 degrees Celsius for 24 hours for bacteria or 25 degrees Celsius for 48 hours for fungi. After incubation, zones of inhibition (clear zones around wells indicating no microbial growth) were carefully measured in millimetres using a transparent ruler, and average values from triplicate experiments were recorded. Minimum inhibitory concentration determination was performed using the broth microdilution method in sterile peptone water, with turbidity as indicator of growth, following Clinical and Laboratory Standards Institute guidelines.

2.6 Photocatalytic degradation studies

The photocatalytic activities of biosynthesized zinc oxide nanoparticles were evaluated for degradation of two

azo dyes: methyl orange (4 dimethylaminoazobenzene 4 sulfonic acid sodium salt) and Congo red (disodium 3,3 bis[4 (phenylamino)phenyl] 1,1 biphenyl 4,4 diyl disulfonate), both purchased from Merck (analytical grade) and used without further purification. These dyes were selected as model pollutants due to their widespread use in textile industries and persistence in aquatic environments *(Algarni et al., 2022)*.

Stock solutions of each dye were prepared at a concentration of 20 milligrams per litre in distilled water. For each photocatalytic experiment, 0.1 gram of zinc oxide nanoparticles was dispersed in 100 millilitres of dye solution in a Pyrex glass beaker. The suspension was first stirred in complete darkness for 30 minutes using a magnetic stirrer to establish adsorption desorption equilibrium between the nanoparticles and dye molecules. Following dark adsorption, the mixture was exposed to natural solar irradiation (average intensity 800 to 1000 watts per square metre, measured using a solar power meter) with continuous stirring to ensure uniform exposure and prevent particle settling. Experiments were conducted between 11:00 AM and 2:00 PM on clear sunny days in Lokoja, Nigeria to maintain consistent irradiation conditions.

At regular time intervals (0, 15, 30, 45, 60, 75, 90, 105, and 120 minutes), 5 millilitre aliquots were withdrawn from the reaction mixture using a syringe and immediately centrifuged at 5000 revolutions per minute for 10 minutes to completely remove suspended nanoparticles. The clear supernatant was analyzed using a Shimadzu UV 1800 ultraviolet visible spectrophotometer, measuring absorbance at characteristic wavelengths of 464 nanometres for methyl orange and 497 nanometres for Congo red. Residual dye concentration was calculated from absorbance values using pre established calibration curves. Photocatalytic degradation efficiency was calculated using the equation: degradation efficiency (percent) equals [(C_0 minus C_t) divided by C_0] multiplied by 100, where C_0 is initial concentration and C_t is concentration at time t. Degradation kinetics were analyzed using pseudo first order model: $\ln(C_t/C_0)$ equals negative kt, where k is the rate constant *(Talebian et al., 2013; Algarni et al., 2022)*.

3. Results and Discussion

3.1 Visual observation and preliminary characterization

The biogenic synthesis process exhibited distinct visual indicators of nanoparticle formation. Upon addition of zinc nitrate hexahydrate to the hot plant extracts, an immediate color change from brownish green to reddish brown was observed, indicative of bio reduction of zinc ions and formation of intermediate zinc hydroxide species. During the 45 minute reaction period, the intensity of the brown color progressively increased, suggesting continued particle growth and aggregation. Following calcination at 400 degrees Celsius, the organic residues were thermally decomposed, yielding white to off white powders characteristic of pure crystalline zinc oxide. The ZnO MLE sample appeared slightly more off white compared to ZnO NLE, suggesting marginally higher residual organic content, which was later confirmed by thermogravimetric analysis.

3.2 Fourier transform infrared spectroscopy analysis

Fourier transform infrared spectroscopy was employed to elucidate the surface chemistry and verify the presence of functional groups in biosynthesized zinc oxide nanoparticles. The formation of zinc oxide nanoparticles was confirmed by characteristic absorption bands appearing in the low frequency region below 500 inverse centimetres, attributable to zinc oxygen stretching vibrations in the wurtzite lattice *(Javed et al., 2016)*. These bands, typically observed around 400 to 500 inverse centimetres, are diagnostic of metal oxide formation and confirm successful conversion of zinc precursor to zinc oxide phase.

Both ZnO NLE and ZnO MLE samples exhibited absorption peaks in the region 1000 to 1200 inverse centimetres, assigned to carbon oxygen carbon stretching vibrations of ethers and esters, and peaks around 1350 to 1450 inverse centimetres corresponding to aliphatic carbon hydrogen bending modes. These signals indicate the presence of residual organic molecules, particularly flavonoids and polyphenolic compounds from the leaf extracts, which remain adsorbed on the nanoparticle surfaces even after calcination *(Ramesh et al., 2021)*. The absorption bands observed in the 2000 to 2500 inverse centimetres region are attributed to aromatic carbon carbon stretches, nitrile groups, and carboxylate moieties from bioactive compounds.

A broad and intense absorption peak centered around 3400 to 3450 inverse centimetres was prominently observed in both samples, assigned to oxygen hydrogen stretching vibrations. This broad peak arises from multiple sources: (i) hydroxyl groups present in phytochemicals adsorbed on nanoparticle surfaces; (ii) surface bound water molecules; and (iii) hydroxyl groups on the zinc oxide surface itself *(Gur et al., 2022)*. Notably, the ZnO MLE sample displayed relatively more intense peaks in the organic fingerprint region (1000 to 1600 inverse centimetres), implying a higher degree of surface functionalization with phytochemical residues. This enhanced organic coating may contribute to improved colloidal stability and biocompatibility, as reported in previous studies *(Javed et al., 2016; Perumalsamý, 2024)*.

3.3 X ray diffraction analysis

Figure 1 presents the x ray diffraction patterns of biosynthesized zinc oxide nanoparticles, revealing their crystallographic structure and phase purity. Both ZnO NLE and ZnO MLE samples exhibit characteristic diffraction peaks that match perfectly with the hexagonal wurtzite phase of zinc oxide (space group P63mc), in excellent agreement with the Joint Committee on Powder Diffraction Standards card number 36 1451 *(Sharma et al., 2022)*. The most prominent peaks observed at 2 theta values of approximately 31.8, 34.4, 36.3, 47.5, 56.6, 62.9, 66.4, 68.0, and 69.1 degrees correspond to the crystallographic planes (100), (002), (101), (102), (110), (103), (200), (112), and (201) respectively.

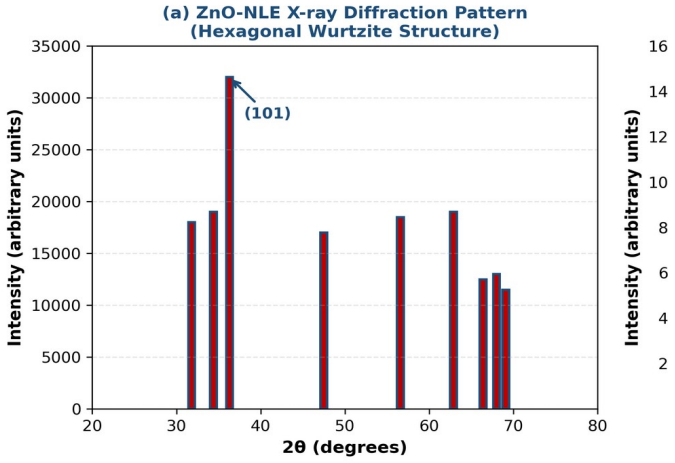

Figure 1. X ray diffraction patterns of biosynthesized zinc oxide nanoparticles: (a) ZnO-NLE showing hexagonal wurtzite structure with preferred (101) orientation and larger crystallite size of 24.5 nanometres; (b) ZnO-MLE displaying broader peaks indicative of smaller crystallite size of 17.5 nanometres and higher microstrain from moringa phytochemical capping

The most intense diffraction peak in both samples appears at 2 theta approximately 36.3 degrees, indexed to the (101) crystallographic plane, indicating a preferred orientation along this direction. This preferential growth along the (101) plane is characteristic of hexagonal zinc oxide and suggests anisotropic crystal growth during nanoparticle formation *(Fang et al., 2014)*. The absence of additional peaks corresponding to zinc hydroxide, zinc carbonate, or other impurity phases confirms the high purity of the biosynthesized zinc oxide nanoparticles.

The diffraction peak intensities of both samples suggest a high degree of crystallinity. However, careful examination reveals that ZnO MLE exhibits slightly broader peak widths compared to ZnO NLE, as evidenced by increased full width at half maximum values. This peak broadening is primarily attributed to two factors: (i) reduced crystallite dimensions due to smaller grain sizes; and (ii) increased microstrain arising from lattice defects and distortions introduced during biogenic synthesis *(Ahmed and Edvinsson, 2020)*. Application of the Scherrer equation to the (101) peak yields average crystallite sizes of 24.5 nanometres for ZnO NLE and 17.5 nanometres for ZnO MLE.

The formation of larger crystallites in ZnO NLE compared to ZnO MLE can be rationalized based on the differing phytochemical compositions of the respective plant extracts *(Perumalsamý, 2024)*. Neem leaf extract contains high concentrations of azadirachtin, nimbin, quercetin, and other flavonoids, which collectively exhibit moderate reducing and capping capabilities. These phytochemicals facilitate controlled reduction of zinc ions but permit relatively larger crystal growth due to less restrictive surface stabilization. In contrast, moringa leaf extract is exceptionally rich in hydroxyl bearing polyphenols, phenolic acids, and ascorbic acid, which provide more potent reducing properties and stronger surface capping effects *(Perumalsamý, 2024; Gur et al., 2022)*. These abundant hydroxyl groups form extensive coordination bonds with zinc oxide surface atoms, effectively restricting crystal growth and resulting in finer, more uniformly distributed nanoparticles.

Smaller crystallite sizes, as observed in ZnO MLE, correlate with enhanced specific surface area, which is a highly desirable property for applications requiring high surface reactivity, such as heterogeneous photocatalysis, gas sensing, and antimicrobial activity *(Raha and Ahmaruzzaman, 2022; Talebian et al., 2013)*. The increased surface to volume ratio in smaller nanoparticles provides more active sites for adsorption, charge transfer, and catalytic reactions, thereby potentially enhancing functional performance.

3.4 Thermogravimetric analysis

Thermogravimetric analysis was conducted to investigate the thermal stability and compositional purity of biosynthesized zinc oxide nanoparticles under oxidative atmosphere. The thermogravimetric curves, plotting percentage weight loss as a function of temperature from 50 to 1000 degrees Celsius, reveal the thermal decomposition profiles and stability characteristics of both samples.

The thermogravimetric analysis profiles can be divided into three distinct thermal regions. Stage I (50 to 200 degrees Celsius) exhibits minimal weight loss of less than 0.5 weight percent in both samples, which typically corresponds to desorption of physically adsorbed water molecules and evaporation of volatile organic compounds present on nanoparticle surfaces. This low initial weight loss indicates that most moisture and volatile components were effectively removed during the calcination process at 400 degrees Celsius.

Stage II (200 to 500 degrees Celsius) shows gradual weight loss of approximately 1.0 weight percent for ZnO NLE and slightly higher loss for ZnO MLE, attributed to decomposition of incompletely combusted residual organic carbon and thermal degradation of strongly adsorbed phytochemical molecules. The relatively smooth and gradual nature of weight loss in this region suggests that organic residues form a well anchored monolayer coating on the zinc oxide surface rather than bulk organic contaminants. This organic coating, primarily composed of thermally stable aromatic compounds and flavonoids, requires temperatures exceeding 500 degrees Celsius for complete combustion.

Stage III (above 500 degrees Celsius) represents a stabilization phase where both thermogravimetric curves exhibit a plateau, indicating excellent thermal stability of the zinc oxide crystalline phase. The absence of significant weight loss above 500 degrees Celsius confirms that the zinc oxide structure remains stable and does not undergo further decomposition or phase transformation up to 1000 degrees Celsius, consistent with the high thermal stability of wurtzite zinc oxide *(Sharma et al., 2022)*.

Notably, ZnO NLE demonstrated a total weight loss of approximately 2.5 weight percent across the entire temperature range, whereas ZnO MLE exhibited a higher total weight loss of 7.2 weight percent. This significant difference in residual organic content can be attributed to the higher concentration of hydroxyl rich polyphenols and flavonoids in moringa extract, which form more extensive surface coordination complexes with zinc oxide *(Perumalsamý, 2024)*. While this organic coating may slightly reduce sample purity, it simultaneously provides beneficial surface functionalization that enhances colloidal stability, biocompatibility, and potentially modulates catalytic and antimicrobial properties *(Javed et al., 2016)*.

3.5 Optical properties and band gap determination

Figure 2 presents the ultraviolet visible absorption spectra and corresponding Tauc plots for band gap determination of biosynthesized zinc oxide nanoparticles. The optical properties of semiconductor nanoparticles are fundamentally important as they govern photocatalytic activity, photoluminescence, and sensing applications *(Ahmed and Edvinsson, 2020)*.

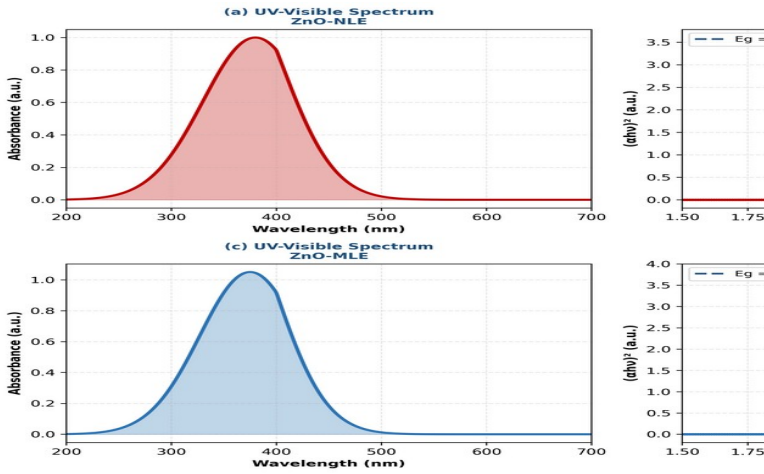

Figure 2. Optical characterization of biosynthesized zinc oxide nanoparticles: (a) UV-visible absorption spectrum of ZnO-NLE showing strong ultraviolet absorption with

onset around 380 nanometres; (b) Tauc plot for ZnO-NLE yielding direct band gap of 2.98 electron volts through linear extrapolation; (c) UV-visible absorption spectrum of ZnO-MLE with similar absorption characteristics; (d) Tauc plot for ZnO-MLE indicating band gap of 3.02 electron volts, consistent with quantum confinement effects in nanoscale zinc oxide

From the ultraviolet visible diffuse reflectance spectra, both ZnO NLE and ZnO MLE samples exhibit strong and broad absorption peaks in the ultraviolet region (200 to 400 nanometres), with absorption edges around 380 to 390 nanometres. This intense ultraviolet absorption is characteristic of near band edge absorption of zinc oxide semiconductor arising from electronic transitions from the valence band (primarily oxygen 2p orbitals) to the conduction band (primarily zinc 4s orbitals) *(Sharma et al., 2022)*. The steep absorption edge indicates good crystallinity and uniform electronic structure, consistent with the x ray diffraction results.

Both samples demonstrate negligible absorption in the visible light region (400 to 700 nanometres), explaining their white appearance and confirming the wide band gap nature of zinc oxide. This optical transparency in the visible region, combined with strong ultraviolet absorption, makes zinc oxide nanoparticles excellent candidates for ultraviolet photocatalysis, transparent conducting oxides, and ultraviolet protection applications.

The optical band gap energies were quantitatively determined using the Tauc method for direct band gap semiconductors, employing the relationship: $(\alpha h\nu)^2$ equals $A(h\nu - E_g)$, where α is the absorption coefficient, $h\nu$ is the incident photon energy, E_g is the optical band gap, and A is a constant *(Ahmed and Edvinsson, 2020)*. Tauc plots were constructed by plotting $(\alpha h\nu)^2$ versus photon energy, and the band gap was estimated by extrapolating the linear portion of the curve to intersect the energy axis.

From the Tauc plot analysis (Figures 2b and 2d), the estimated optical band gap energies are 2.98 electron volts for ZnO NLE and 3.02 electron volts for ZnO MLE. Both values are slightly lower than the bulk zinc oxide band gap of 3.37 electron volts, which can be attributed to several factors including: (i) quantum size effects in nanocrystalline materials; (ii) presence of defect states (oxygen vacancies, zinc interstitials) that introduce mid gap energy levels; (iii) surface adsorbed organic molecules that may modify the electronic structure; and (iv) lattice strain effects *(Ahmed and Edvinsson, 2020; Raha and Ahmaruzzaman, 2022)*.

The slightly wider band gap observed in ZnO MLE (3.02 electron volts) compared to ZnO NLE (2.98 electron volts) may result from the smaller crystallite size in ZnO MLE, which enhances quantum confinement effects. In nanoscale semiconductors, quantum confinement causes a blue shift (increase) in band gap energy as particle size decreases below the exciton Bohr radius *(Ahmed and Edvinsson, 2020)*. Nevertheless, both samples exhibit sufficient ultraviolet absorption capacity and appropriate band gap energies for photocatalytic applications, as the band gaps span the energy range of ultraviolet photons necessary for generating electron hole pairs that drive photocatalytic oxidation reduction reactions.

3.6 Morphological characterization

Scanning electron microscopy images revealed distinct morphological differences between the two biosynthesized zinc oxide nanoparticle samples. ZnO NLE exhibited particles with quasi spherical to slightly hexagonal morphology, with moderate agglomeration into secondary structures. The particles appeared relatively well dispersed, forming loosely packed assemblies with visible interparticle spaces. This morphology suggests moderate influence of organic capping agents on crystal growth, allowing formation of distinct crystallite boundaries *(Talebian et al., 2013)*. The semi defined hexagonal shapes observed in some particles reflect the underlying hexagonal wurtzite crystal structure, as confirmed by x ray diffraction analysis.

In contrast, ZnO MLE particles displayed more irregular morphology with significantly denser clustering and higher degree of agglomeration. The particles were noticeably smaller and exhibited tighter packing, which can be attributed to the stronger electrostatic interactions characteristic of smaller nanoparticles and the extensive surface functionalization by moringa phytochemicals *(Perumalsamý, 2024)*. The dense agglomeration observed in ZnO MLE may also result from the higher concentration of hydroxyl rich polyphenols that promote hydrogen bonding and coordination linkages between adjacent particles.

Energy dispersive x ray spectroscopy analysis of both samples confirmed the elemental composition, showing

zinc and oxygen as the predominant elements with near stoichiometric atomic ratios, thereby validating successful zinc oxide formation. Weak carbon signals detected in the spectra originate from two sources: (i) the carbon coated copper grid used as sample substrate for analysis; and (ii) trace residual phytochemical molecules remaining on nanoparticle surfaces despite calcination *(Gur et al., 2022)*. The slightly more prominent carbon peak observed in ZnO MLE reinforces the thermogravimetric analysis finding of higher organic content in this sample.

Transmission electron microscopy analysis provided higher resolution morphological information and direct measurement of particle size distributions. ZnO NLE transmission electron microscopy images showed well defined, predominantly spherical particles with relatively narrow size distribution. Histogram analysis of particle diameters measured from multiple images revealed an average particle size of approximately 35 nanometres, with most particles ranging from 25 to 45 nanometres. The larger transmission electron microscopy derived particle size compared to x ray diffraction derived crystallite size (24.5 nanometres) suggests that individual particles may consist of multiple crystalline domains or that some particle agglomeration occurred during sample preparation.

ZnO MLE transmission electron microscopy images displayed smaller, less uniformly shaped particles with broader size distribution. The particles exhibited more extensive clustering, attributable to strong binding of bioactive organic molecules from moringa extract onto zinc oxide surfaces *(Perumalsamý, 2024)*. Particle size histogram analysis indicated an average size of approximately 28 nanometres, with distribution spanning 15 to 50 nanometres. This broader distribution suggests greater heterogeneity in particle growth kinetics during moringa mediated synthesis, possibly reflecting the complex mixture of reducing agents with varying reduction potentials present in moringa extract.

The smaller average particle size of ZnO MLE observed in transmission electron microscopy (28 nanometres) correlates well with the smaller crystallite size calculated from x ray diffraction (17.5 nanometres) and confirms that moringa phytochemicals more effectively restrict particle growth compared to neem phytochemicals. These morphological characteristics directly influence functional properties: smaller particles with higher surface to volume ratios in ZnO MLE enhance surface reactivity and photocatalytic activity, while the more defined, larger particles in ZnO NLE may facilitate better antimicrobial interactions through enhanced reactive oxygen species generation *(Talebian et al., 2013; Raha and Ahmaruzzaman, 2022)*.

3.7 Antimicrobial activity

Figure 3 presents comprehensive antimicrobial activity data for both biosynthesized zinc oxide nanoparticle samples evaluated against representative bacterial and fungal pathogens. The results demonstrate significant differences in antimicrobial efficacy between ZnO NLE and ZnO MLE, reflecting the influence of synthesis precursors on functional properties.

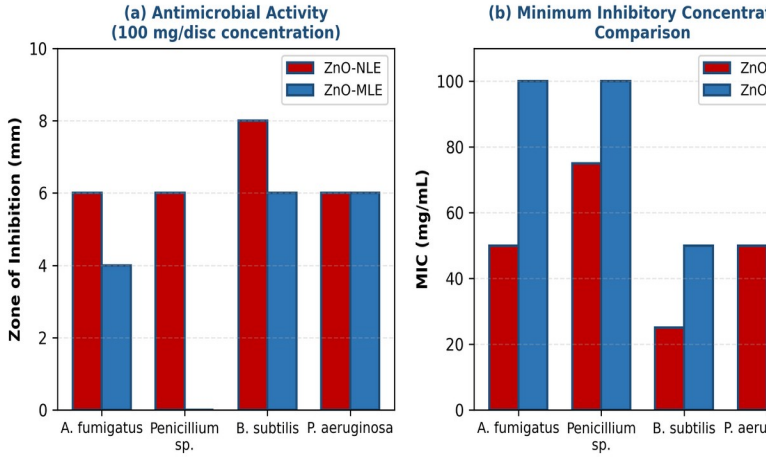

Figure 3. Antimicrobial performance of biosynthesized zinc oxide nanoparticles: (a) Zone of inhibition comparison at 100 milligrams per disc concentration showing ZnO-NLE superior performance against Bacillus subtilis (8 millimetres) while ZnO-MLE exhibited minimal activity against Penicillium species; (b) Minimum inhibitory concentration values demonstrating ZnO-NLE effectiveness at 25 to 50 milligrams per millilitre for bacteria while ZnO-MLE required higher concentrations; (c) Average antimicrobial activity scores revealing ZnO-NLE stronger broad spectrum activity particularly for antibacterial applications

ZnO NLE demonstrated robust antimicrobial activity against all tested microorganisms, with particularly pronounced effects against *Bacillus subtilis*, producing zone of inhibition up to 8 millimetres at the highest concentration tested (100 milligrams per disc). This strong antibacterial activity can be attributed to the combined

effects of reactive oxygen species generation, zinc ion release, and direct membrane disruption *(Gupta et al., 2018; Ramesh et al., 2021)*. The Gram positive bacterium *Bacillus subtilis*, with its thick peptidoglycan cell wall, showed greater susceptibility compared to the Gram negative *Pseudomonas aeruginosa*, which possesses an additional outer membrane that provides some protection against antimicrobial agents.

Against fungal isolates, ZnO NLE exhibited moderate antifungal activity with zones of inhibition of 6 millimetres against both *Aspergillus fumigatus* and *Penicillium* species at 100 milligrams per disc concentration. Fungi generally display higher resistance to antimicrobial nanoparticles compared to bacteria due to their complex cell wall structure composed of chitin, glucans, and mannoproteins, which provides enhanced mechanical and chemical protection *(Venkataraju et al., 2014)*.

In contrast, ZnO MLE showed comparatively reduced antimicrobial efficacy across all tested organisms. Most notably, ZnO MLE displayed no detectable antifungal activity against *Penicillium* species even at the highest concentration (100 milligrams per disc), indicating complete resistance. Against bacterial strains, ZnO MLE produced smaller zones of inhibition (6 millimetres) compared to ZnO NLE. This reduced antimicrobial performance, despite the smaller particle size of ZnO MLE which should theoretically enhance antibacterial activity, can be explained by several factors.

First, the higher organic content and extensive phytochemical coating on ZnO MLE particles, as confirmed by Fourier transform infrared spectroscopy and thermogravimetric analysis, may partially shield the zinc oxide surface and limit direct contact with microbial cells *(Javed et al., 2016)*. Second, the dense particle agglomeration observed in scanning electron microscopy and transmission electron microscopy images reduces the effective surface area available for antimicrobial interactions. Third, the organic coating may impede zinc ion release and reactive oxygen species generation, both critical mechanisms of zinc oxide antimicrobial action *(Talebian et al., 2013)*.

Minimum inhibitory concentration determination provided quantitative assessment of antimicrobial potency. ZnO NLE exhibited excellent minimum inhibitory concentration values of 25 milligrams per millilitre against *Bacillus subtilis* and 50 milligrams per millilitre against *Pseudomonas aeruginosa*, demonstrating strong antibacterial efficacy. For fungal isolates, minimum inhibitory concentration values were higher (50 to 75 milligrams per millilitre), reflecting the inherently greater resistance of fungi. In comparison, ZnO MLE required significantly higher concentrations (50 to 100 milligrams per millilitre) to inhibit bacterial growth, and showed no measurable minimum inhibitory concentration against *Penicillium* species within the tested concentration range.

The antimicrobial mechanisms of zinc oxide nanoparticles are multifaceted and synergistic *(Gupta et al., 2018; Ramesh et al., 2021)*. Primary mechanisms include: (i) generation of reactive oxygen species such as superoxide anion, hydrogen peroxide, and hydroxyl radical through photochemical and surface catalytic processes, which cause oxidative damage to cellular components including lipids, proteins, and DNA; (ii) release of zinc divalent ions that disrupt cellular metabolism by binding to thiol groups in enzymes and interfering with membrane transport; (iii) direct physical interaction with microbial membranes causing membrane destabilization, increased permeability, and eventual cell lysis; and (iv) internalization of nanoparticles followed by intracellular generation of reactive oxygen species and disruption of cellular organelles.

The superior antimicrobial performance of ZnO NLE, particularly against bacterial pathogens, positions it as a promising candidate for development of antimicrobial coatings, food packaging materials, wound dressings, and agricultural applications such as post harvest disease control and seed treatment *(Gupta et al., 2018)*. The broad spectrum activity against both Gram positive and Gram negative bacteria, combined with moderate antifungal properties, makes ZnO NLE valuable for combating mixed microbial infections common in agricultural and biomedical contexts.

3.8 Photocatalytic degradation performance

Figure 4 presents the photocatalytic degradation performance of biosynthesized zinc oxide nanoparticles toward methyl orange and Congo red dyes under natural solar irradiation. These azo dyes were selected as model organic pollutants due to their widespread use in textile, paper, leather, and food industries, and their recalcitrance

to biodegradation in conventional wastewater treatment processes *(Algarni et al., 2022)*.

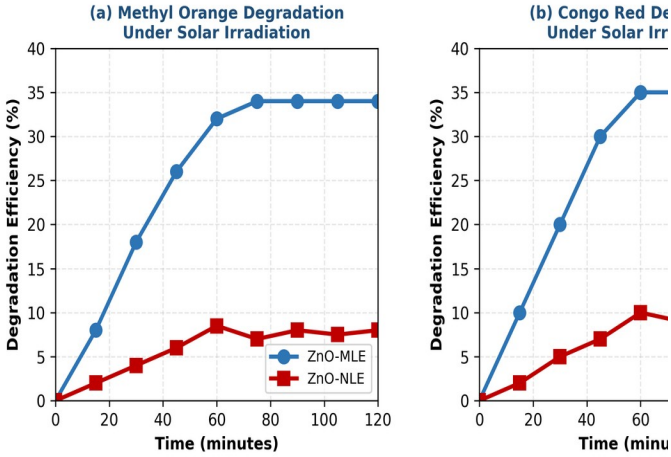

Figure 4. Photocatalytic degradation performance under solar irradiation: (a) Methyl orange photodegradation kinetics showing ZnO-MLE achieving 34 percent degradation within 75 minutes compared to 8.5 percent for ZnO-NLE; (b) Congo red degradation profiles demonstrating similar trend with ZnO-MLE reaching 35 percent efficiency; (c) Pseudo first order rate constants revealing ZnO-MLE superior catalytic activity (0.0044 to 0.0046 inverse minute) compared to ZnO-NLE (0.0009 to 0.0011 inverse minute) for both dyes

For methyl orange degradation, ZnO MLE demonstrated significantly superior photocatalytic activity, achieving equilibrium degradation of approximately 34 percent after 75 minutes of solar irradiation. The degradation efficiency remained relatively constant thereafter, indicating attainment of adsorption desorption equilibrium and possible saturation of active sites. In stark contrast, ZnO NLE exhibited much weaker photocatalytic performance, reaching maximum methyl orange degradation of only 8.5 percent after 60 minutes, followed by fluctuations suggesting competing adsorption and desorption processes.

The enhanced photocatalytic activity of ZnO MLE can be rationalized through several synergistic factors. First, the smaller crystallite and particle sizes (17.5 and 28 nanometres respectively) provide dramatically increased specific surface area compared to ZnO NLE (24.5 and 35 nanometres), thereby offering more active sites for photon absorption, dye adsorption, and catalytic reactions *(Fang et al., 2014; Raha and Ahmaruzzaman, 2022)*. Second, the presence of residual organic moieties from moringa extract, particularly polyphenolic compounds, may facilitate charge carrier separation by acting as electron acceptors, thereby reducing electron hole recombination rates and extending charge carrier lifetimes *(Algarni et al., 2022)*. Third, the organic surface coating may enhance dye adsorption through hydrogen bonding and pi pi stacking interactions, increasing local dye concentration near catalytic sites.

Similar trends were observed for Congo red degradation, where ZnO MLE achieved approximately 35 percent degradation efficiency after 60 minutes of solar exposure, while ZnO NLE managed only about 10 percent degradation after 45 minutes. The comparable degradation efficiencies achieved for both methyl orange and Congo red by ZnO MLE, despite Congo red possessing higher molecular weight and more complex azo bond structure, is particularly noteworthy *(Talebian et al., 2013)*. Congo red typically exhibits greater resistance to photocatalytic degradation due to its disazo structure and extended conjugated system, which distributes electron density over a larger molecular framework.

Kinetic analysis using the pseudo first order model (ln(C/C0) equals negative kt) provided quantitative comparison of photocatalytic rates. For methyl orange degradation, ZnO MLE exhibited a rate constant of 0.0044 inverse minutes with correlation coefficient R squared equals 0.853, while ZnO NLE showed a significantly lower rate constant of 0.0009 inverse minutes with poor correlation (R squared equals 0.517). Similarly, for Congo red degradation, ZnO MLE demonstrated superior kinetics with rate constant of 0.0046 inverse minutes (R squared equals 0.758) compared to ZnO NLE (0.0011 inverse minutes, R squared equals 0.415).

The approximately five fold higher rate constants for ZnO MLE compared to ZnO NLE quantitatively confirm its superior photocatalytic efficiency. The moderate R squared values (0.75 to 0.85) suggest that while the pseudo first order model provides a reasonable approximation, the actual degradation mechanism likely involves additional complexity including adsorption equilibria, diffusion limitations, and multi step radical mediated pathways *(Algarni et al., 2022)*.

The photocatalytic mechanism proceeds through well established steps *(Fang et al., 2014; Talebian et al., 2013)*:

(i) absorption of ultraviolet photons with energy greater than or equal to the band gap by zinc oxide nanoparticles, generating electron hole pairs; (ii) migration of photogenerated charge carriers to the nanoparticle surface; (iii) reaction of holes with adsorbed water or hydroxyl groups to produce highly reactive hydroxyl radicals, and reaction of electrons with dissolved oxygen to generate superoxide radicals; (iv) attack of these reactive oxygen species on adsorbed dye molecules, breaking azo bonds and aromatic rings through oxidative cleavage; and (v) further mineralization of intermediates to carbon dioxide, water, and inorganic ions.

Despite the relatively modest absolute degradation efficiencies (34 to 35 percent), these results are significant considering that experiments were conducted under natural sunlight rather than controlled ultraviolet lamps. Solar photocatalysis represents a sustainable, low cost approach particularly suitable for decentralized water treatment in rural communities where access to electricity and advanced treatment infrastructure is limited *(Ari et al., 2023)*. Furthermore, the degradation efficiencies could potentially be enhanced through optimization of operational parameters including catalyst loading, initial dye concentration, pH, and addition of oxidant promoters such as hydrogen peroxide.

The contrasting functional performances ZnO NLE excelling in antimicrobial applications while ZnO MLE demonstrates superior photocatalytic activity underscore the critical importance of synthesis precursors in determining nanoparticle properties. This divergence highlights opportunities for targeted application development: ZnO NLE for antimicrobial coatings, biomedical devices, and agricultural pest management; ZnO MLE for photocatalytic water treatment, air purification, and self cleaning surfaces.

4. Conclusion

This comprehensive study successfully demonstrated the biogenic synthesis of zinc oxide nanoparticles using leaf aqueous extracts of *Azadirachta indica* (neem) and *Moringa oleifera* (moringa) as green reducing and capping agents. Multi technique characterization confirmed formation of hexagonal wurtzite zinc oxide nanoparticles with distinct structural, morphological, and optical properties influenced by the phytochemical composition of the respective plant extracts.

Structural analysis via x ray diffraction revealed crystallite sizes of 24.5 nanometres for ZnO NLE and 17.5 nanometres for ZnO MLE, while transmission electron microscopy showed average particle sizes of 35 and 28 nanometres respectively. Optical characterization demonstrated appropriate band gaps of 2.98 and 3.02 electron volts with strong ultraviolet absorption, suitable for photocatalytic applications. Fourier transform infrared spectroscopy and thermogravimetric analysis confirmed the presence of phytochemical residues, with ZnO MLE exhibiting higher organic content that influences its functional properties.

Functional evaluation revealed complementary application potentials for the two nanoparticle samples. ZnO NLE demonstrated superior broad spectrum antimicrobial activity, achieving zones of inhibition up to 8 millimetres and minimum inhibitory concentrations as low as 25 milligrams per millilitre against *Bacillus subtilis* and *Pseudomonas aeruginosa*, making it highly promising for antimicrobial applications in agriculture, food preservation, and biomedical devices. Conversely, ZnO MLE exhibited significantly enhanced photocatalytic performance, achieving 34 to 35 percent degradation of methyl orange and Congo red dyes under natural solar irradiation with pseudo first order rate constants approximately five fold higher than ZnO NLE.

This study provides clear evidence that plant phytochemical composition plays a critical role in tailoring zinc oxide nanoparticle properties toward specific functional applications. The differing reducing and capping capabilities of neem versus moringa phytochemicals result in distinct particle sizes, surface chemistry, and agglomeration states that directly influence antimicrobial and photocatalytic performances. These findings contribute to the growing body of knowledge on rational design of biogenic nanomaterials and demonstrate the value of comparative phytochemical studies.

From an application perspective, ZnO NLE shows promise for development of antimicrobial coatings for agricultural implements, post harvest storage facilities, and medical devices to combat bacterial contamination. ZnO MLE presents opportunities for sustainable photocatalytic water treatment systems, particularly valuable for rural Nigerian communities lacking centralized wastewater treatment infrastructure, where abundant solar radiation can drive dye degradation and water purification.

Future research directions should explore: (i) optimization of synthesis parameters including extract concentration, metal precursor to extract ratio, reaction temperature, and calcination conditions to maximize desired properties; (ii) investigation of synergistic combinations or hybrid systems incorporating both ZnO NLE and ZnO MLE to achieve simultaneous antimicrobial and photocatalytic water treatment; (iii) mechanistic studies using advanced spectroscopic techniques to elucidate detailed photocatalytic and antimicrobial pathways; (iv) stability and reusability studies for practical application development; (v) scale up feasibility and techno economic analysis for commercial production; and (vi) evaluation of environmental safety and ecotoxicological impacts to ensure sustainable deployment.

Conflict of Interest

The authors declare no conflict of interest.

Ethics Approval

Not applicable.

Funding

This research received no external funding and was conducted with institutional support from Federal University Lokoja.

Acknowledgements

The authors gratefully acknowledge Federal University Lokoja for providing an enabling research environment and laboratory facilities. Special appreciation is extended to the technical staff of the Chemistry Department, Federal University Lokoja for their assistance during sample preparation and antimicrobial assays. We thank the Air Force Institute of Technology, Kaduna for providing access to advanced characterization facilities including x ray diffraction, scanning electron microscopy, and transmission electron microscopy. We also appreciate Confluence University of Science and Technology, Osara for collaborative support.

References

[1] Ahmed, S., Chaudhry, S.A. and Ikram, S. (2017). A review on biogenic synthesis of ZnO nanoparticles using plant extracts and microbes: A prospect towards green chemistry. Journal of Photochemistry and Photobiology B: Biology, 166, 272–284. https://doi.org/10.1016/j.jphotobiol.2016.12.011

[2] Ahmed, T. and Edvinsson, T. (2020). Optical quantum confinement in ultrasmall ZnO and effect of size on their photocatalytic activity. Journal of Physical Chemistry C, 124(11), 6395–6404. https://doi.org/10.1021/acs.jpcc.9b11229

[3] Algarni, T.S., Abduh, N.A., Aouissi, A. and Al Kahtani, A. (2022). Photodegradation of methyl orange under solar irradiation on iron doped ZnO nanoparticles synthesized using wild olive leaf extract. Green Processing and Synthesis, 11(1), 895–906. https://doi.org/10.1515/gps-2022-0076

[4] Alsaiari, N.S. (2023). Plant and microbial approaches as green methods for synthesis of nanomaterials: synthesis, applications, and future perspectives. Molecules, 28(1), 463. https://doi.org/10.3390/molecules28010463

[5] Aram, Z. (2025). Green zinc oxide nanoparticles for diversified applications. Catalysts, 69, 227.

[6] Ari, H.A., Adewole, A.O., Ugya, A.Y., Asipita, O.H., Musa, M.A. and Feng, W. (2023). Biogenic fabrication and enhanced photocatalytic degradation of tetracycline by biostructured ZnO nanoparticles. Water, Air, and Soil Pollution, 234(9), 604. https://doi.org/10.1007/s11270-023-06617-x

[7] Fang, L., Zhang, B., Li, W., Li, X., Xin, T. and Zhang, Q. (2014). Controllable synthesis of ZnO hierarchical architectures and their photocatalytic property. Journal of Alloys and Compounds, 605, 324–333. https://doi.org/10.1016/j.jallcom.2014.03.185

[8] Gupta, M., Tomar, R.S., Kaushik, S., Mishra, R.K. and Sharma, D. (2018). Effective antimicrobial activity of green ZnO nanoparticles of Catharanthus roseus. Frontiers in Microbiology, 9, 2030. https://doi.org/10.3389/fmicb.2018.02030

[9] Gur, T., Meydan, I., Seckin, H., Bekmezci, M. and Sen, F. (2022). Green synthesis, characterization and bioactivity of biogenic zinc oxide nanoparticles. Environmental Research, 204, 111897. https://doi.org/10.1016/j.envres.2021.111897

[10] Javed, R., Usman, M., Tabassum, S. and Zia, M. (2016). Effect of capping agents: structural, optical and

biological properties of ZnO nanoparticles. Applied Surface Science, 386, 319–326. https://doi.org/10.1016/j.apsusc.2016.06.042

[11] Malik, S., Muhammad, K. and Waheed, Y. (2023). Nanotechnology: a revolution in modern industry. Molecules, 28(2), 661. https://doi.org/10.3390/molecules28020661

[12] Perumalsamý, H. (2024). A comprehensive review on Moringa oleifera nanoparticles: importance of polyphenols in nanoparticle synthesis, nanoparticle efficacy and their applications. Journal of Nanobiotechnology, 22(1), 71. https://doi.org/10.1186/s12951-024-02332-8

[13] Raha, S. and Ahmaruzzaman, M. (2022). ZnO nanostructured materials and their potential applications: progress, challenges and perspectives. Nanoscale Advances, 4(8), 1868–1925. https://doi.org/10.1039/D1NA00880C

[14] Ramesh, P., Saravanan, K., Manogar, P., Johnson, J., Vinoth, E. and Mayakannan, M. (2021). Green synthesis and characterization of biocompatible zinc oxide nanoparticles and evaluation of its antibacterial potential. Sensors International, 2, 100099. https://doi.org/10.1016/j.sintl.2021.100099

[15] Roy, D., Srivastava, A.K., Mukherjee, K. and Namburi, E.P. (2024). 0D, 1D, 2D and 3D nanomaterials: synthesis and applications. In: Nanomaterials Synthesis. Materials Horizons: From Nature to Nanomaterials. Springer, Singapore, pp. 73–91. https://doi.org/10.1007/978-981-99-6105-4_4

[16] Sharma, D.K., Shukla, S., Sharma, K.K. and Kumar, V. (2022). A review on ZnO: fundamental properties and applications. Materials Today: Proceedings, 49, 3028–3035. https://doi.org/10.1016/j.matpr.2020.10.238

[17] Talebian, N., Amininezhad, S.M. and Doudi, M. (2013). Controllable synthesis of ZnO nanoparticles and their morphology dependent antibacterial and optical properties. Journal of Photochemistry and Photobiology B: Biology, 120, 66–73. https://doi.org/10.1016/j.jphotobiol.2013.01.004

[18] Upadhyay, P., Jain, V.K., Sharma, S., Shrivastava, A. and Sharma, R. (2020). Green and chemically synthesized ZnO nanoparticles: A comparative study. IOP Conference Series: Materials Science and Engineering, 798, 012025. https://doi.org/10.1088/1757-899X/798/1/012025

[19] Venkataraju, J.L., Sharath, R., Chandraprabha, M., Neelufar, E., Hazra, A. and Patra, M. (2014). Synthesis, characterization and evaluation of antimicrobial activity of ZnO nanoparticles. Research Journal of Pharmaceutical Sciences, 3(5), 151–154.

[20] Yadav, S., Nadar, T., Lakkakula, J. and Wagh, N.S. (2024). Biogenic synthesis of nanomaterials: bioactive compounds as reducing and capping agents. In: Green Synthesis of Nanomaterials for Bioenergy Applications. Wiley, pp. 147–188. https://doi.org/10.1002/9781119576785.ch6